

# Gemini Frontier Fields: Wide-field Adaptive Optics $K_s$ -band Imaging of the Galaxy Cluster MACS J0416.1-2403<sup>1</sup>

M. Schirmer<sup>1</sup>, R. E. Carrasco<sup>1</sup>, P. Pessev<sup>1</sup>, V. Garrel<sup>1</sup>, C. Winge<sup>1</sup>, B. Neichel<sup>2,1</sup>, F. Vidal<sup>3,1</sup>

<sup>1</sup>*Gemini Observatory, Casilla 603, La Serena, Chile*

<sup>2</sup>*Aix Marseille Université, CNRS, Laboratoire d'Astrophysique de Marseille, UMR 7326, 13388, Marseille, France*

<sup>3</sup>*Observatoire De Paris, Place Jules Janssen, 92190 Meudon, France*

mschirme@gemini.edu

## ABSTRACT

The Hubble Space Telescope (HST) Frontier Fields Campaign targets six massive clusters of galaxies, exploiting the strong gravitational lensing effect to study the distant Universe. At Gemini South we observe the three southern-most clusters in  $K_s$ -band, overcoming HST/WFC3's sensitivity cut-off redwards of  $1.7\mu\text{m}$ . We use the Gemini Multi-Conjugate Adaptive Optics System (GeMS) and the Gemini South Adaptive Optics Imager (GSAOI), delivering near diffraction-limited images on arcminute scales. In this paper we describe our public release of  $100'' \times 110''$  wide images of the first target, MACS J0416.1-2403. With a  $5\sigma$  depth of  $K_s \sim 23.8$  mag for extended sources our images are shallower than the HST/WFC3 data. Yet we have achieved an angular resolution of  $0'.07-0'.10$ , twice as high as HST/WFC3, using a single natural guide star only. The data were distortion corrected and registered with sub-pixel accuracy despite only a few low-S/N extended sources are visible in the individual exposures. This is a demonstration that even for fields at high galactic latitude, where natural guide stars are scarce, current multi-conjugated adaptive optics technology at 8m-telescopes has opened a new window on the distant Universe. We provide fully calibrated, co-added images matching the native GSAOI pixel scale as well as the larger plate scales and the WCS projections of the HST release. Two more Frontier Fields, Abell 2744 and Abell S1063, will be observed with GeMS/GSAOI, adding to the legacy value of this community effort.

*Subject headings:* Techniques: image processing, Instrumentation: adaptive optics, Galaxies: Clusters: individual (MACS J0146.1-2403)

## 1. Introduction

The HST Frontier Fields campaign combines deep observations of six massive galaxy clusters in the optical and the infrared, using the Advanced Camera for Surveys (ACS) and WFC3, respectively.

<sup>1</sup>Based on observations obtained at the Gemini Observatory, which is operated by the Association of Universities for Research in Astronomy, Inc., under a cooperative agreement with the NSF on behalf of the Gemini partnership: the National Science Foundation (United States), the Science and Technology Facilities Council (United Kingdom), the National Research Council (Canada), CONICYT (Chile), the Australian Research Council (Australia), Ministério da Ciência, Tecnologia e Inovação (Brazil) and Ministerio de Ciencia, Tecnología e Innovación Productiva (Argentina).

The magnification effect from strong gravitational lensing in these clusters provides a unique opportunity for studies of the galaxy population in the young Universe. The wavelength coverage with HST/ACS and HST/WFC3 ranges from  $0.43\mu\text{m}$  to  $1.6\mu\text{m}$ . Complementary observations have been obtained with Chandra (PI: Murray, S.), Spitzer (PIs: Soifer, T., Capak, P.), Subaru/SuprimeCam (Postman et al. 2011), VLT/HAWK-I (Owers et al. 2011) and AAT/AAOmega (Ebeling et al. 2014).

HST/WFC3 is insensitive for wavelengths longer than  $1.7\mu\text{m}^2$ . This design was chosen to allow for

<sup>2</sup>[http://www.stsci.edu/hst/nicmos/documents/handbooks/current\\_NEW/c04\\_imaging.6.8.html](http://www.stsci.edu/hst/nicmos/documents/handbooks/current_NEW/c04_imaging.6.8.html)

Table 1: Summary of the observing nights. See Sect. 2 for details.

Night	$\alpha_{J2000}$	$\delta_{J2000}$	Exposures	$\Delta_{RZP}$ [mag]	$\sigma_{RZP}$ [mag]	$\langle \text{AO seeing} \rangle$	Nat. seeing
2014-01-13	04:16:07.8	-24:05:05	40 $\times$ 120s	+0.02	0.016	0'076	0'4-0'7
2014-01-14	04:16:07.8	-24:05:05	37 $\times$ 120s	-0.02	0.014	0'077	0'6-0'9
2014-01-19	04:16:06.6	-24:04:47	34 $\times$ 120s	-0.09	0.040	0'175	0'9-1'1
2014-01-20	04:16:06.6	-24:04:47	47 $\times$ 120s	+0.04	0.015	0'103	0'5-0'9
2014-01-22	04:16:06.6	-24:04:47	16 $\times$ 120s	+0.04	0.032	0'105	0'5-0'7

simpler thermo-electric cooling of the detector, and because HST itself contributes to the thermal background, which approaches that of ground-based observatories at  $\gtrsim 2\mu\text{m}$ . While the Earth's atmosphere offers a suitable observing window between  $2.0\mu\text{m}$  and  $2.3\mu\text{m}$  ( $K_s$ -band), its turbulence limits the resolution and the depth with classical imaging. Using multi-conjugated adaptive optics (MCAO) (Ragazzoni et al. 2000; Ellerbroek & Rigaut 2000), these adverse effects can be overcome for fields as large as one arcminute or more. In theory, diffraction limited observations are possible, given a sufficient number of bright natural guide stars (NGS) and a good laser return for the artificial laser guide stars (LGS). Nowadays, such wide-field diffraction limited observations can be obtained in the infrared at Gemini South with GeMS<sup>3</sup> (Rigaut et al. 2014; Neichel et al. 2014b) and the GSAOI<sup>4</sup> (McGregor et al. 2004; Carrasco et al. 2012) camera.

GeMS is the first MCAO system in use at an 8m telescope. It delivers an uniform, close to diffraction-limited near-infrared image over a  $2'$  field. GeMS uses five sodium LGS and needs three NGS to compensate for tip-tilt and plate-dynamical errors (plate scale variations). To achieve optimum performance, the NGS should be positioned as close as possible to an equilateral triangle about the science target. Best constellations (*asterisms*) are the ones that cover most of the field. The larger the angular separations between the stars become, the lower the plate scale error will be. Unfortunately, this condition is usually not met for high galactic latitude fields with low stellar density. With sub-optimal asterisms the PSF will become non-uniform. This is the case for MACS J0416.1-2403, where only one sufficiently bright NGS is available. Nevertheless we have achieved 70 – 100 milli-arcsecond image seeing, surpassing that of HST/WFC3 by a factor of two.

<sup>3</sup><http://www.gemini.edu/sciops/instruments/gems/>

<sup>4</sup><http://www.gemini.edu/sciops/instruments/gsaoui/>

The focus in the remainder of this paper is on the observations (Section 2), and on various data reduction aspects such as background modeling and astrometry (Section 3). In Section 4 we summarize the properties of the coadded images and describe the data release.

## 2. Observations

MACS J0416.1-2403 was observed with GSAOI on five nights between 2014-01-13 and 2014-01-22, using director's discretionary time (Program ID: GS-2013B-DD-1). Figure 1 shows the area covered by GSAOI in comparison to the HST observations and the area with high magnification expected for a  $z = 9$  source (Richard et al. 2014). GSAOI is a near-infrared adaptive optics camera designed to work with GeMS. Its focal plane is formed by a  $2 \times 2$  mosaic of Hawaii-2RG  $2048 \times 2048$  pixel arrays with  $3''0$  wide gaps. Images are recorded in a  $85'' \times 85''$  field of view with a plate scale of  $0'0197 \text{ pixel}^{-1}$ . The individual exposure times of our  $K_s$ -band images were 120s. A  $3 \times 3$  dither pattern with  $7''$  step size (in some cases  $14''$ ) covers the gaps between the detector arrays. The same dither pattern was repeated several times without shift of the base position. Data processing has revealed that this strategy does not allow to entirely suppress background residuals and cross-talk (see Sect. 3).

The vicinity of MACS J0416.1-2403 offers only one suitably bright NGS. To optimize the observations, the NGS was located outside the GSAOI field of view, but within the patrol field area of GeMS. Due to an error in the setup of the observations (the NGS is a high proper motion star), the images observed during the first two nights were recorded with a South-Eastern offset of  $24''$ . As a result, the NGS appears in one of the four arrays. The images recorded during the other three nights have the correct base position.

The observing log is presented in Table 1. The UT dates and the coordinates of the base positions are listed in columns 1, 2 and 3, respectively. The num-

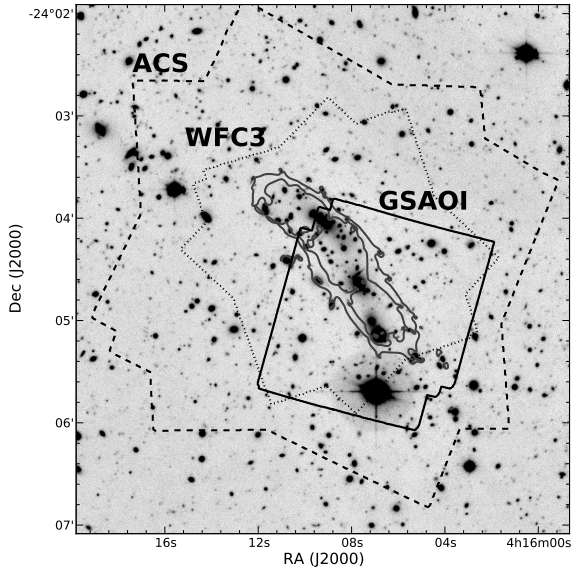


Fig. 1.— Layout of the HST/ACS, HST/WFC3 and GSAOI fields for MACS J0416.1-2403. The grey contours indicate the area where a magnification higher than 20 is expected for a  $z = 9$  source.

ber of images and their individual exposure time are given in column 4. Column 5 shows the mean relative sky transparency between the nights, and column 6 the *rms* scattering of the relative zero-points between exposures (see also Sect. 3.6 and Fig. 8). The last two columns, 7 and 8, show the average corrected AO FWHM, measured using IRAF/imexam, and the natural seeing recorded by the DIMM, respectively. 2014-01-19 was significantly worse than the other nights, having about 0.1 mag less transparency and only 0'17 average AO-corrected seeing (due to higher natural seeing). Data from that night was only included in the low resolution stack (see Sect. 4).

### 3. Data reduction

All data processing stpdf were performed with THELI (Schirmer 2013; Erben et al. 2005). We followed the stpdf in Appendix B of Schirmer (2013), consisting of flat fielding, a two-pass background subtraction, weighting, individual sky subtraction and coaddition. In the following, we explain where and why we deviated from that scheme.

### 3.1. Background modeling

A regular  $3 \times 3$  dither pattern with 7'' step size was used for images observed on 2014-01-13/14, repeated consecutively without offsetting the base position. For images observed on 2014-01-19/20/22, a dither pattern with 7'' and 14'' step size was used. To remove most of the background signal from an individual exposure, a floating median was calculated from the 8 nearest exposures in time. In a first pass, these exposures were combined without masking to get rid of the bulk of the sky signal. In a second pass, THELI uses *SExtractor* (Bertin & Arnouts 1996) to compute object masks for the median combination. Without these masks the fainter halos of the cluster galaxies would bias the background model to higher values, leading to dark halos in the coadded image. We have found that this two-pass approach fell short, as the *SExtractor* masks were still too small.

We have therefore added a module to THELI that optionally extends the object masks. This module uses an alternative parametrization of the best-fit ellipse to an object's isophotes. A pixel with image coordinates  $x$  and  $y$  is located inside the ellipse if

$$C_{XX}(x - \bar{x})^2 + C_{YY}(y - \bar{y})^2 + C_{XY}(x - \bar{x})(y - \bar{y}) \leq R^2, \quad (1)$$

where  $\bar{x}$  and  $\bar{y}$  represent the object's centroid (first moment), and  $C_{XX}$ ,  $C_{YY}$  and  $C_{XY}$  are *SExtractor* parameters calculated from the second brightness moments. A choice of  $R \sim 3$  would usually represent the outer isophote of a detection<sup>5</sup>. Only for  $R = 8$  or higher the over-correction of the sky disappeared in the co-added images. This *mask expansion* is available in THELI as of v2.9.0, with  $R$  being referred to as the *mask expansion factor*. It can be selected during background modeling, collapse correction (see below), and individual sky subtraction. Figure 2 illustrates the effect.

Note that very extended (i.e. larger than the dither pattern) features of low surface brightness, such as intra-cluster light, still escape this masking process, and are therefore suppressed in the co-added images. This can only be avoided if the observing strategy includes interspersed blank sky fields, reducing the effective on-target time.

### 3.2. Reset anomaly and background gradients

GSAOI shows an unstable reset anomaly in array #2. Its origin has not yet been determined, but is prob-

<sup>5</sup>For details see the *SExtractor* user manual v2.13, Sect. 10.1.6)

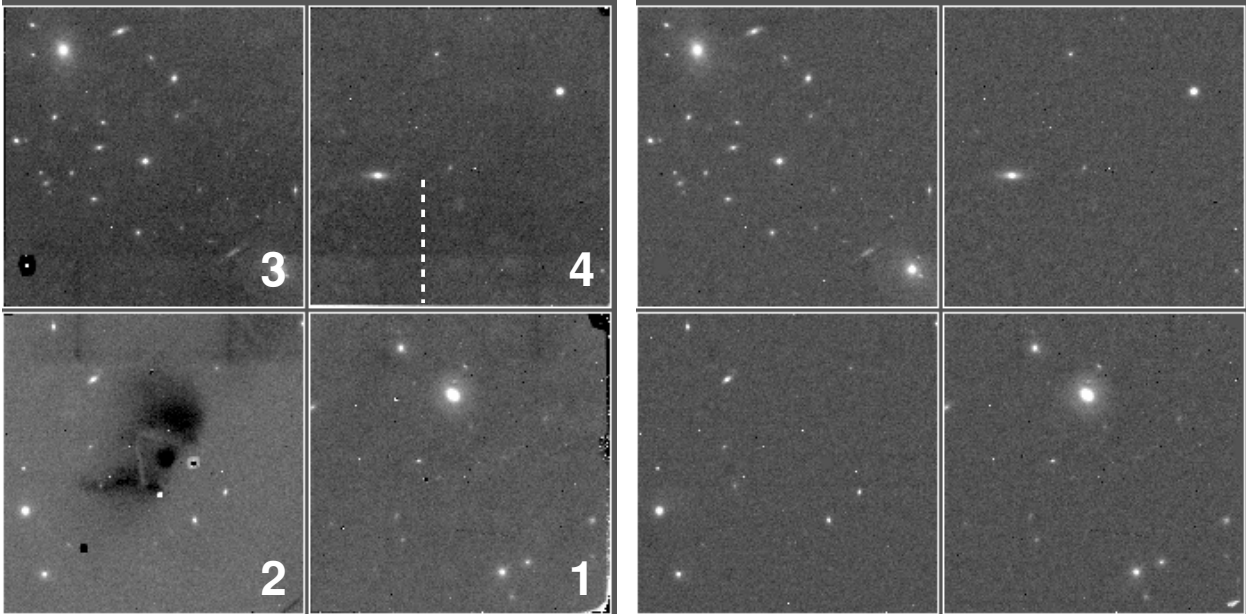


Fig. 3.— Left: The four GSAOI detector arrays (labeled). A reset anomaly (dark extended spot) appears in array #2 at the beginning of each observing sequence. Independently, horizontal striping with a low amplitude occurs in  $\geq 80\%$  of exposures, affecting all four detectors. We illustrate the latter by plotting the mean row values along the dashed white line in array #4 both before and after correction (see Fig. 4). Right: Same exposure after correction for reset anomaly and striping. Note that this is a high contrast display of  $12 \times 12$  binned data, exaggerating the effects.

ably due to a bias/dark problem in the detector controller. Every first image in an exposure series is affected by it, as well as the image taken immediately after an interruption of the series (e.g. because of the laser being shuttered for air planes or satellites). The anomaly is evident in the data after background subtraction as described in Sect. 3.1. We corrected for it by median combining all affected images from this array, and then subtracted the model from the data after rescaling. The rescaling factors were determined manually and ranged between 0.2 and 1.3. The pattern was removed entirely from the data (see Fig. 3).

In addition to the reset anomaly, and independent of it, horizontal stripes are found in 84% of our GSAOI data. They run parallel to the interface between arrays #2/3 and #1/4 (see Figs. 3 and 4). Both the amplitude and the angular extent of the stripes vary from exposure to exposure. They affect an identical number of rows in all four arrays, but on a much less significant extent than the reset anomaly. In our data, in the worst case, their amplitude reaches 0.2% of the background level, and is 3 – 4 times smaller than the sky noise. Yet this will impact the smoothness of the background in a

co-added image constructed from many exposures. We correct for it on an exposure by exposure basis, by averaging all columns in an array, and then subtract this mean column from all columns (*collapse correction* in THELI). Prior to the averaging process all objects in the exposures are masked as described in Sect. 3.1.

### 3.3. Sky subtraction

The background modeling using a floating median described in Sect. 3.1 still leaves some background pedestal in the data. This is because the images used for the correction were taken over about 40 minutes, and thus temporal sky variations are not sampled closely. We correct for these on an exposure by exposure basis, masking all objects as describe previously, but this time using a very conservative mask expansion factor of  $R = 20$ . The masked pixels are then interpolated from their neighboring unmasked pixels, after which we convolve the image with a Gaussian kernel and subtract it from the original. Best results in terms of preserving faint extended galaxy halos while minimizing larger background residuals were obtained for a 150 pixel or  $3''$  wide Gaussian kernel.

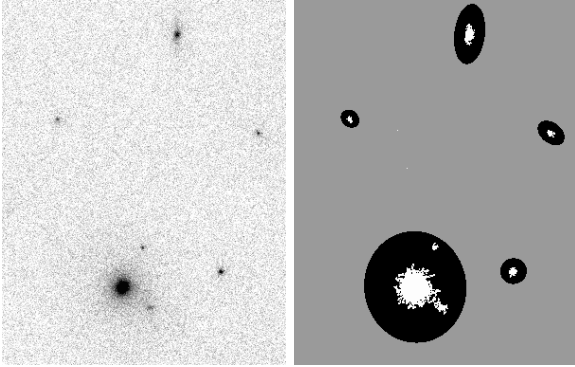


Fig. 2.— Expansion of object masks to avoid biasing of the background models by faint galaxy halos. Left: Part of a GSAOI image after the first pass background subtraction. Right: *SExtractor* mask before (white) and after (black) mask expansion with  $R = 8$ , using `DETECT_THRESH=1.2` and `DETECT_MINAREA=20`.

### 3.4. Image persistence and crosstalk

Saturated objects leave a weak imprint in subsequent GSAOI exposures (image persistence). In the case of MACS J0416.1-2403, the only saturating source is a bright field star (Fig. 1), leaving a charge residual of  $\sim 0.2\%$ . We have masked these ghosts manually in the weight images as they did not average out entirely (because of the repeated dither pattern).

The same star, located in array #1, also causes a significant negative crosstalk footprint in one of the four output channels of array #1. Contrary to image persistence, the position of this crosstalk is fixed with respect to the star and thus does not average out. It was masked and is thus absent in the released images.

Other memory effects exist in some GSAOI arrays. This is particularly noticeable in the low resolution ( $0''.06 \text{ pixel}^{-1}$ ) stacked image, which has a high signal-to-noise ratio due to the effective  $3 \times 3$  re-binning. Therein, darker spots mirror the dithering. The spots have a maximum amplitude of about twice the background noise level (Fig. 5). Only few and rather localised parts of the arrays are affected, as neighboring sources of similar brightness do not cause ghosting. We have not corrected for this effect. It should be a minor concern for most analyzes as it rarely coincides with images of astrophysical objects. A non-repetitive dither pattern would have suppressed this feature.

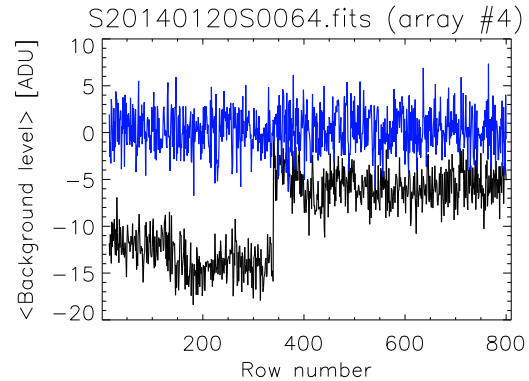


Fig. 4.— Mean row values before (black line) and after (blue line) correction for striping. The data was extracted along the dashed line shown in Fig. 3.

## 3.5. Astrometric calibration

### 3.5.1. Astrometry with wide-field AO data

Astrometry with GSAOI is non-trivial for three reasons. First, there is a large discrepancy between the angular resolutions of GSAOI and common all-sky astrometric reference catalogs. In case of dense stellar fields several sources may be found in the GSAOI data within the error circle of the astrometric reference source. Second, the AO field of view is small, such that at high galactic latitude no (or only a few) reference sources are found. Third, GeMS introduces a significant field distortion by means of its optical relay (consisting of two off-axis parabolic mirrors). Fortunately, this distortion is static and, as we show below, it can be measured reliably even for sparse data. A smaller variable distortion component exists that is dominated by instrument flexure due to a changing gravity vector (Neichel et al. 2014a). This effect becomes important when high precision relative astrometry (on the order of one milli-arcsecond and below) is required across the field (Neichel et al. 2014a,b).

### 3.5.2. GSAOI astrometry with *SExtractor* and *Scamp*

The most important step toward successful WCS matching and distortion modeling of GSAOI data with *THELI* is to provide a deeper secondary or even tertiary reference catalog (Schirmer 2013). The latter must have matching resolution and sufficient depth. In case of MACS J0416.1-2403 we have used the HST/ACS F814W image, as (1) it fully covers the GSAOI data (WFC3 does not), and (2) it is an excellent match in

Instrument A1: distortion map

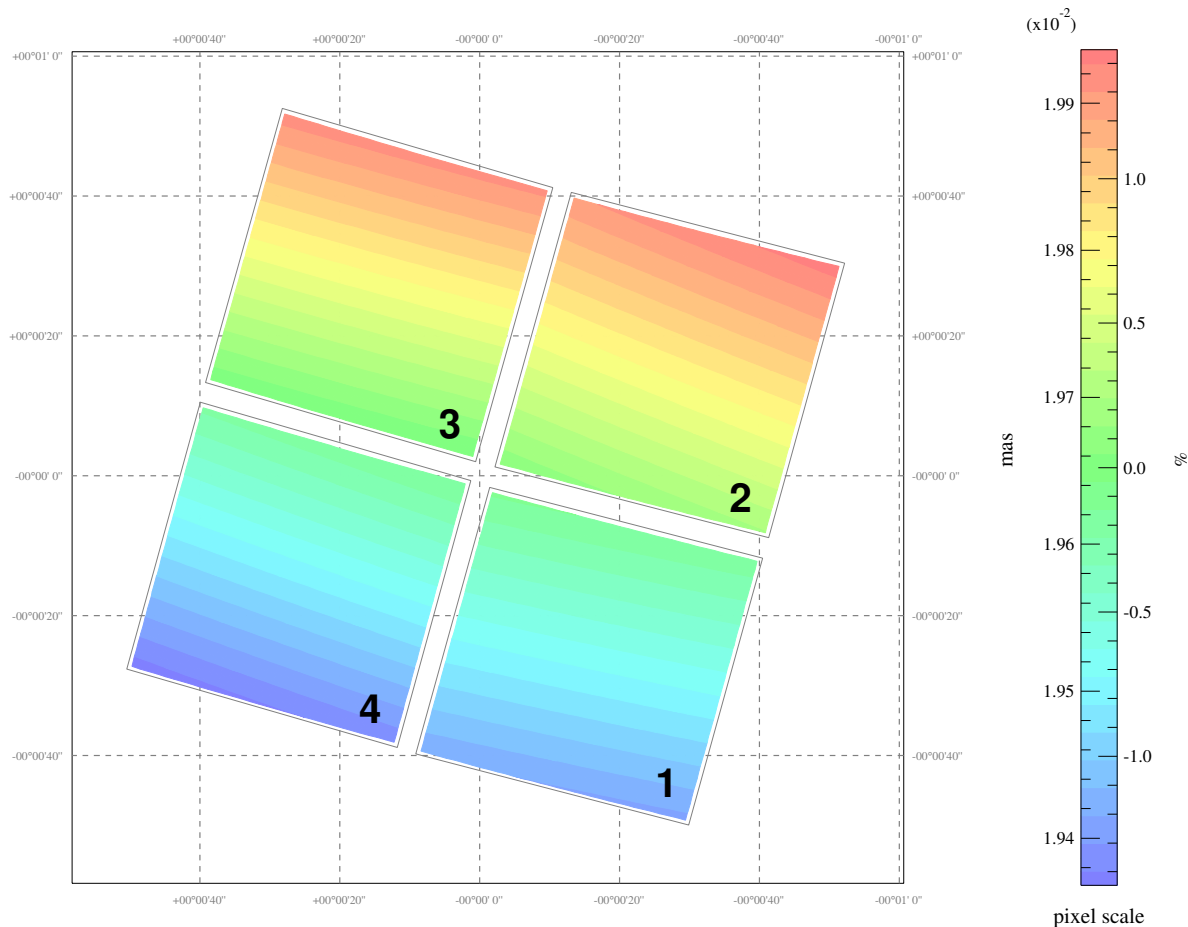


Fig. 6.— Typical GSAOI distortion for one night, calculated with *Scamp*. A linear model was chosen to describe the variation of the plate scale across each of the four arrays. Note that *Scamp* calculates the distortion model independently for each array. The distortion is recovered reliably from the dithered data despite the low source density.

terms of angular resolution.<sup>6</sup>

Before the astrometric calibration could be attempted, we had to manually correct the CRVAL1/2 FITS keywords in the data from 2014-01-13/14. The setup error described in Sect. 2 resulted in an offset of  $\sim 24''$  for these nights, which is not reflected in the headers of the archival data. This offset proved too large to be automatically recognized by *Scamp* (Bertin 2006), which THELI uses for the astrometric calibration. Normally, the WCS in the GSAOI headers is accurate to  $1''$  or better.

<sup>6</sup>We note that a ground-based reference image taken with the 2.2m MPG/ESO telescope was also used successfully for the astrometry.

We fed *SExtractor* source catalogs into *Scamp*, using a low threshold per pixel (DETECT.THRESH=1.2) to maximize the number of detections. A minimum of DETECT.MINAREA=20 pixels above this threshold was required to form a valid object (rejecting spurious sources, and because GSAOI data are oversampled). This resulted in an average of  $13 \pm 6$  detections per array, one or none of them being stars.

For our data, *Scamp* (v2.0.1) delivers the best results if the matching to the reference catalog has been explicitly separated from the distortion correction. In a first step we thus calculated a zero order WCS solution. This included (1) a refined median estimate of the

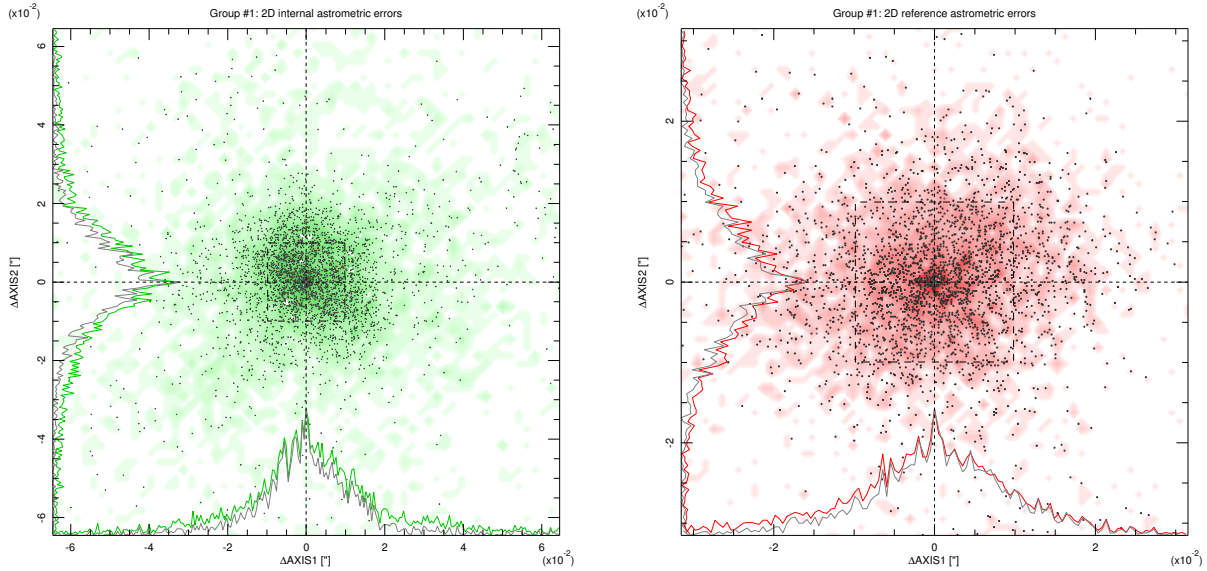


Fig. 7.— Astrometric residuals. Shown are the internal residuals (i.e. between exposures, left panel) and the external residuals (with respect to the HST/ACS F814W image; right panel). Sub-pixel accuracy is achieved in both cases, despite only a few dozen low-S/N detections of extended sources have been available for the calibration.

relative chip positions and orientations from all exposures in a night (`MOSAIC_TYPE = FIX_FOCALPLANE`), and (2) the calculation of the images’ individual CD matrices and `CRVAL1/2`. Allowing for just a linear change in pixel scale would already result in some arrays being incorrectly matched. We updated the WCS in the FITS headers and recreated the source catalogs. Then *Scamp* was run a second time, with distortion correction switched on and matching switched off. We reproduce the relevant parameter settings in Table 2. A typical (linear) distortion model is shown in Fig. 6, revealing a variation of pixel scale of nearly 3%.

We have successfully applied this procedure with *Scamp* to many other GSAOI data sets, ranging from dense stellar fields (solved with higher order distortion polynomials) to very sparse extragalactic areas.

### 3.5.3. Internal and external astrometric accuracy

Neither the internal (between exposures) nor the external residuals (with respect to the reference catalog) were reduced when switching from a linear change of the pixel scale (`DISTORT_DEGREE = 2` in *Scamp*) to a quadratic change (`DISTORT_DEGREE = 3`). The quadratic solutions appeared more unstable, which is not surprising given the low number of sources available to constrain the fit. As the fits were indistinguish-

able in the  $\chi^2$  sense, we have chosen the simpler linear hypothesis (Fig. 6). The internal and external residuals are shown in Fig. 7 and measure 9 and 6 milli-arcseconds, respectively. This is equivalent to half a GSAOI pixel or better and should be sufficient for this particular data set and its scientific applications.

The dominating factors limiting the fit are the low source density and the large measurement uncertainties of the source centroids (0.1 – 0.3 pixels or 2 – 6 milli-arcseconds for galaxies). The centroids are much better determined in the reference catalog constructed from the high S/N HST/ACS F814W image, which explains the lower external residuals. The accuracy of the absolute astrometry is entirely limited by the WCS of the public HST/ACS F814 image (their v1.0 release).

Our astrometric solutions have been obtained on a nightly basis. We have also tested (1) a common distortion model for all nights, and (2) separate solutions for smaller chunks of data to evaluate the impact of flexure changes. The common distortion model had an inferior fit with increased  $\chi^2$ . This is because the large angular offsets between the base positions of different nights have introduced different distortion patterns as the NGS and LGS configurations move with respect to each other (Neichel et al. 2014a,b; Rigaut et al. 2014). For the second test we have split the nightly

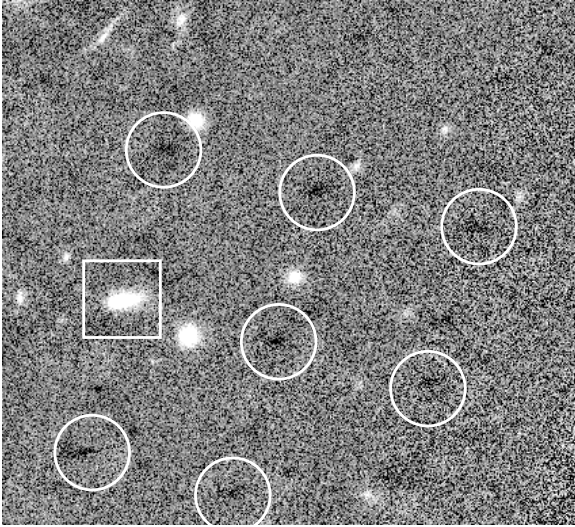


Fig. 5.— A low-level memory effect (white circles) with negative amplitude is present in certain areas of the co-added data. In this example it is caused by the galaxy marked with a white square. A neighbouring object of similar brightness does not trigger the effect.

sequences into blocks of 30 minutes to better sample the flexure changes. We find that for blocks with good AO-corrected seeing (80 milli-arcseconds) the internal residuals decrease from 9 to 7 milli-arcseconds for a linear fit, whereas for other blocks the quality of the fit was unchanged or worse. We thus decided to use the more stable nightly fits instead.

Better performances are hard to reach with GeMS at high galactic latitude with few low S/N detections per array, almost all of which extended, and just a single NGS. In comparison, for dense stellar fields such as NGC 1851 with 500 – 1000 sources per array with  $S/N > 10 - 100$ , optimal NGS asterisms and in the absence of dithering, GeMS delivers relative astrometric accuracies of 0.4 milli-arcseconds and better (Neichel et al. 2014a; Ammons et al. 2013; Rigaut et al. 2012).

### 3.6. Photometric calibration

THELI normalizes the gains of multi-chip cameras to the array with the lowest gain, i.e. array #2 in case of GSAOI. The co-added images are scaled in  $\text{ADU s}^{-1}$ . The Vega-based photometric zero-points reported below must be seen in this context.

Table 2: *Scamp* parameters for our two-step approach

Parameter	1st pass	2nd pass
POSANGLE_MAXERR	0.5	0.5
POSITION_MAXERR	0.04	0.04
PIXSCALE_MAXERR	1.03	1.03
DISTORT_DEGREE	1	2
ASTREF_WEIGHT	3	3
STABILITY_TYPE	INSTRUMENT	INSTRUMENT
MOSAIC_TYPE	FIX_FP	FIX_FP
CROSSID_RADIUS	1'0	0'3
MATCH	Y	N

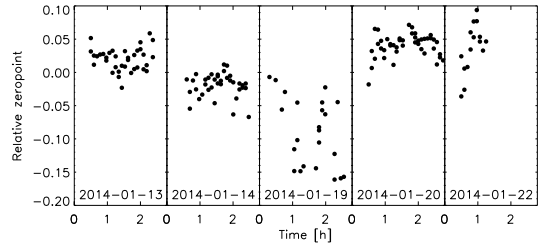


Fig. 8.— Variation of the relative photometric zero-points (RZP), indicating non-photometric conditions.

#### 3.6.1. Transparency

Sky transparency was good, yet unstable during all observing nights, with relative zero-points scattering by up to  $\pm 0.05$  mag within a night. We also report systematic offsets of  $^{+0.02}_{-0.03}$  mag between the nights (see Fig. 8 and Table 1). The instabilities were caused by a high inversion layer trapping significant amounts of humidity above the observatory. Such conditions may be difficult to recognize at night by observers. Other factors that contribute to the scattering between exposures are errors in the gain determination of the four arrays of 0.5% – 1.0%, and small differences in their quantum efficiencies. In Carrasco et al. (2012) we have observed similar uncertainties for various stellar and non-stellar fields.

#### 3.6.2. Absolute zero-point

For the absolute photometric calibration two standards from the MKO catalog (Leggett et al. 2006) were observed on 2014-01-13 at airmasses 1.13 and 1.35, 1h and 4h after the last science exposure was taken. Assuming that the mean transparency has not changed after the science observations, we derive a photometric

Table 3: Summary of the released co-added data. The FWHM is the average seeing measured within  $1'$  of the NGS.

Stack name	Filter	Pixel scale	$t_{\text{exp}}$ [s]	FWHM	Geometry [pix].
MACS_J0416.1-2403_GSAOI_0.02_deep.fits	$K_s$	$0'.02$	15720	$0'.085$	$6920 \times 6780$
MACS_J0416.1-2403_GSAOI_0.02_seeing.fits	$K_s$	$0'.02$	6600	$0'.077$	$6920 \times 6780$
MACS_J0416.1-2403_GSAOI_0.03_deep.fits	$K_s$	$0'.03$	15720	$0'.086$	$10000 \times 10000$
MACS_J0416.1-2403_GSAOI_0.03_seeing.fits	$K_s$	$0'.03$	6600	$0'.080$	$10000 \times 10000$
MACS_J0416.1-2403_GSAOI_0.06_deep.fits	$K_s$	$0'.06$	18600	$0'.095$	$5000 \times 5000$

zero-point (Vega) of  $ZP = 25.62 \pm 0.06$  mag (MAGZP and MAGZPER keyword in the FITS headers). This value is based on a linear two parameter fit for the zero-point and the extinction coefficient. We have set the color term to zero, as the GSAOI  $K_s$  filter is in the same MKO system as the standards of Leggett et al. (2006). The uncertainty of 0.06 mag is a conservative error estimate. It includes the nominal uncertainty of the fit, contributions from the non-photometric conditions and the uncertainties of the detector characteristics. For comparison, the only non-saturated star in the area detected by 2MASS has a  $K_s$ -band magnitude of 15.36 mag after transformation to the MKO system, compared to 15.42 mag measured in our data. This is just within our  $1\sigma$  error bar.

On 2014-01-14/20 standards from Persson et al. (1998) were observed, which are in a different filter systems with color terms on the order of 3%. These nights were as unstable as 2014-01-13, and no superior photometric solution was found. A refined zero-point will be provided with a future data release, based on an external calibration with the Flamingos-2 near-infrared imager at Gemini South. The corresponding observations have been scheduled already.

### 3.6.3. Limiting magnitude

The depth of the co-added exposures is difficult to determine. Only a few point sources are found, none of which is near the detection limit. Instead, we look at compact (yet extended) galaxies with half-light radii  $\leq 0'.15$  in the deep medium resolution stack (see Sect. 4). Based on the distribution of magnitude errors, we measure a  $10\sigma$  detection limit of  $K_s = 22.4 \pm 0.2$  mag and extrapolate a  $5\sigma$  limit of  $23.8 \pm 0.4$  mag.

## 4. Summary and data release

The Gemini Frontier Fields Campaign complements HST/WFC3 observations redwards of  $1.7\mu\text{m}$  for the three southern-most clusters. Using GeMS/GSAOI,

the first MCAO system in use at an 8m telescope, near diffraction-limited images on angular scales larger than  $1'$  are obtained in  $K_s$ -band. We make the fully calibrated co-added images and weights publicly available<sup>7</sup>. In this paper we describe the observations and data reduction of the first cluster observed, MACS J0416.1-2403. Co-added images for Abell 2744 and Abell S1063 will be made available as soon as the data have been obtained and processed.

We release different co-added images resampled to  $0'.02$ ,  $0'.03$  and  $0'.06$  pixel<sup>-1</sup> (high, medium and low resolution stacks). The first preserves the native pixel scale of GSAOI, whereas the other two use identical plate scales, WCS projections and image geometries as the HST data release (their v1.0).

Natural seeing conditions have varied during the observing nights. Thus we provide two different versions for the high and medium resolution stacks, optimized for seeing (35% of all exposures) and depth (85%). For the low resolution stack only one deep version is provided comprised of all usable exposures, as PSF anisotropies and softer seeing become insignificant in this undersampled image. Table 3 summarizes the key properties of all released data.

Only one NGS is available for GeMS/GSAOI near MACS J0416.1-2403. This results in increasing PSF variations and FWHM as a function of separation from the NGS (Fig. 10). The performance variation over the field is predicted well based on numerical simulations, which are available in the Gemini Observing Tool<sup>8</sup>. With a FWHM of  $0'.07$ – $0'.10$  we improve upon HST/WFC3's angular resolution by a factor of two, albeit over a smaller field of view ( $100'' \times 110''$ ). We reach a  $5\sigma$  depth for extended sources of  $K_s^{\text{lim}} = 23.8$  mag. This demonstrates that MCAO at Gemini South works well even for high galactic latitude fields where

<sup>7</sup><http://www.gemini.edu/sciops/instruments/gsaoi/public-data>

<sup>8</sup><http://www.gemini.edu/sciops/instruments/gems/gems-performance?q=node/11864#Asterism.visualization>

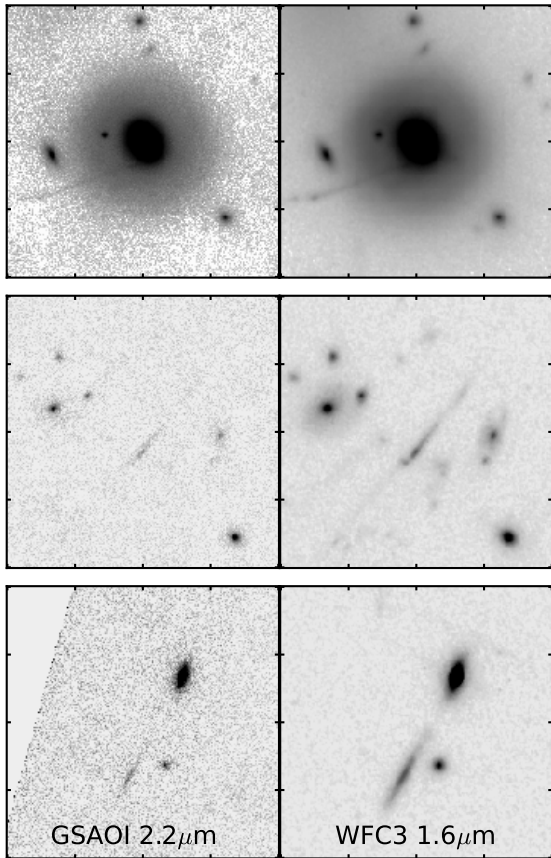


Fig. 9.— Comparison of strongly lensed features seen by GSAOI and HST/WFC3. The areas measure  $12'' \times 12''$ , and have North up and East left.

natural guide stars are scarce, opening a new window onto the distant Universe. We also show that current data reduction techniques, developed for classical imaging, are well suitable to process and align such data with inherent very low source densities.

### Acknowledgments

We thank Nancy Levenson and Markus Kissler-Patig for granting us directors' discretionary time for this program. This work utilizes gravitational lensing models produced by PIs Brada, Ebeling, Merten & Zitrin, Sharon, and Williams funded as part of the HST Frontier Fields program conducted by STScI. STScI is operated by the Association of Universities for Research in Astronomy, Inc. under NASA contract NAS 5-26555. The lens models were obtained from

the Mikulski Archive for Space Telescopes (MAST).

### REFERENCES

- Ammons, S. M., Bendek, E., Guyon, O., et al. 2013, in Proceedings of the Third AO4ELT Conference, ed. S. Esposito & L. Fini
- Bertin, E. 2006, in ASP Conf. Ser., Vol. 351, ADASS XV, ed. C. Gabriel, C. Arviset, D. Ponz, & S. Enrique, 112
- Bertin, E. & Arnouts, S. 1996, *A&AS*, 117, 393
- Carrasco, E. R., Edwards, M. L., McGregor, P. J., et al. 2012, in Society of Photo-Optical Instrumentation Engineers (SPIE) Conference Series, Vol. 8447, Society of Photo-Optical Instrumentation Engineers (SPIE) Conference Series
- Ebeling, H., Ma, C.-J., & Barrett, E. 2014, *ApJS*, 211, 21
- Ellerbroek, B. & Rigaut, F. 2000, *Nature*, 403, 25
- Erben, T., Schirmer, M., Dietrich, J., et al. 2005, *AN*, 326, 432
- Leggett, S. K., Currie, M. J., Varricatt, W. P., et al. 2006, *MNRAS*, 373, 781
- McGregor, P., Hart, J., Stevanovic, D., et al. 2004, *Proc. SPIE*, 5492, 1033
- Neichel, B., Lu, J. R., Rigaut, F., et al. 2014a, *ArXiv e-prints*
- Neichel, B., Rigaut, F., Vidal, F., et al. 2014b, *MNRAS*, 440, 1002
- Owers, M. S., Randall, S. W., Nulsen, P. E. J., et al. 2011, *ApJ*, 728, 27
- Persson, S. E., Murphy, D. C., Krzeminski, W., Roth, M., & Rieke, M. J. 1998, *AJ*, 116, 2475
- Postman, M., Coe, D., Ford, H., et al. 2011, in Bulletin of the American Astronomical Society, Vol. 43, American Astronomical Society Meeting Abstracts #217, 227.06
- Ragazzoni, R., Marchetti, E., & Valente, G. 2000, *Nature*, 403, 54
- Richard, J., Jauzac, M., Limousin, M., et al. 2014, *MNRAS*, 444, 268

Rigaut, F., Neichel, B., Boccas, M., et al. 2012,  
in Society of Photo-Optical Instrumentation  
Engineers (SPIE) Conference Series, Vol.  
8447, Society of Photo-Optical Instrumentation  
Engineers (SPIE) Conference Series

Rigaut, F., Neichel, B., Boccas, M., et al. 2014,  
MNRAS, 437, 2361

Schirmer, M. 2013, ApJS, 209, 21

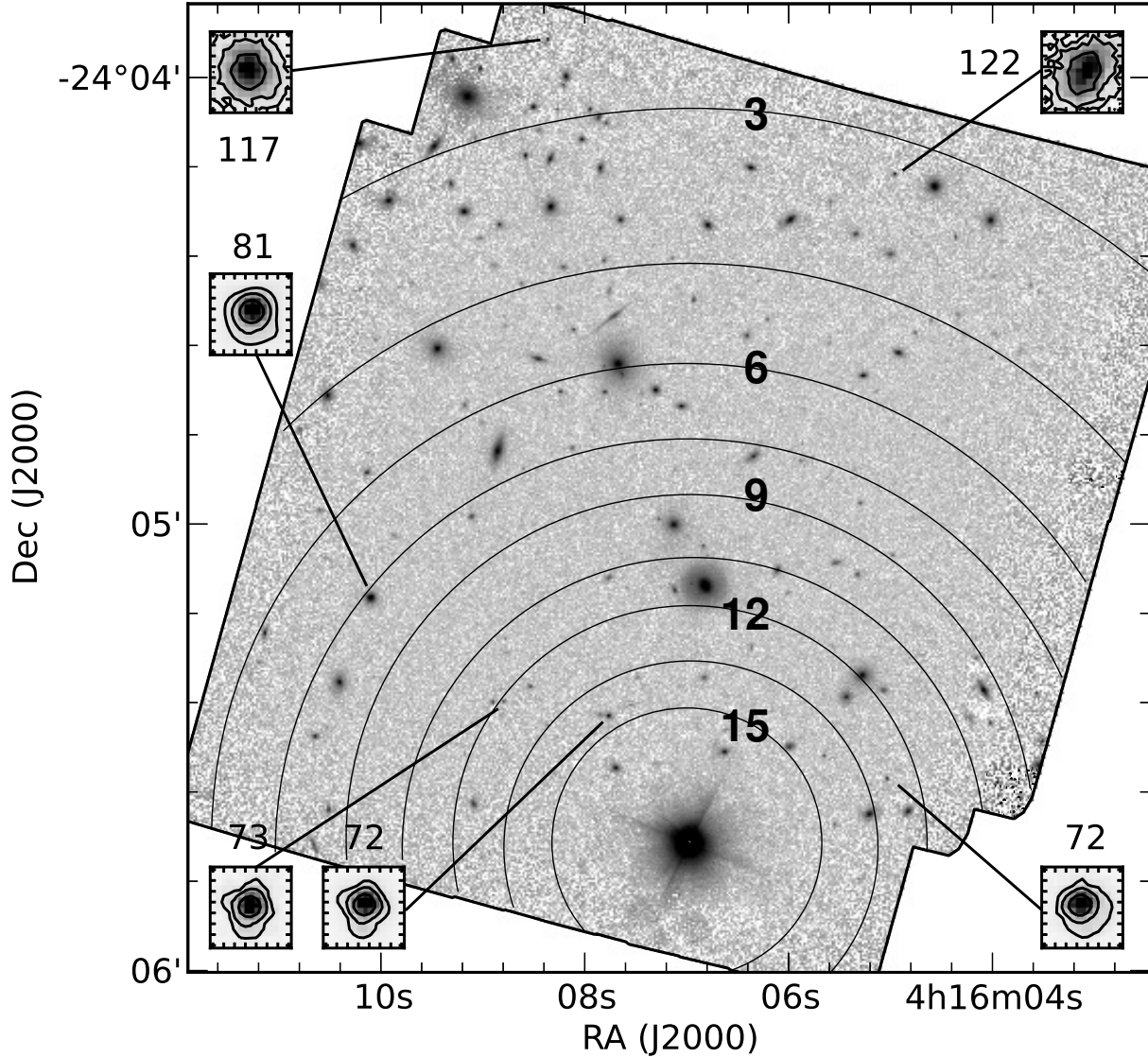


Fig. 10.— PSF of the 6 brightest field stars in our medium resolution *good seeing* stack. The extent of the small boxes is  $0''.3 \times 0''.3$ , and the contour levels therein correspond to 0.1, 0.2 and 0.5 times the stars' peak fluxes. The PSF is fairly uniform and increases with growing distance from the single natural guide star (bright source at the bottom). Only the upper right star displays significant ellipticity. The numeric values next to each box correspond to the direct FWHM in milli-arcseconds, measured with IRAF/imexam. The large concentric contours around the natural guide star show the expected Strehl ratio for the given guide configuration, increasing from 3% to 15%. The expected average Strehl ratio is 6.9%, corresponding to a FWHM of 90 mas, consistent with the delivered image quality. For reference, the diffraction limited FWHM for GeMS/GSAOI in  $K_s$ -band is 55 milli-arcseconds (Neichel et al. 2014b).